CMOS Active Pixel Sensor Specific Performance Effects on Star Tracker/Imager Position Accuracy

Bruce R. Hancock, Robert C. Stirbl, Thomas J. Cunningham,

Bedabrata Pain, Chris J. Wrigley, Peter G. Ringold

Jet Propulsion Laboratory, California Institute of Technology, Pasadena, CA 91109

ABSTRACT

This paper gives the status of theoretical and experimental efforts at *JPL* in the development of environmentally robust (Radiation Hard and Radiation Tolerant), ultra-low power, high performance CMOS active pixel sensor (APS) imagers for star tracker/imager applications. The work explores the effect of imager performance on star position accuracy, specifically examining the performance of JPL designed APS imagers. Accuracy is estimated as a function of star magnitude for a nominal star tracker optical design. Using these APS sensors, which have wide dynamic range and no blooming, simultaneous imaging of widely differing star magnitudes during the same observation is possible. It is shown that prototype Rad Hard APS imagers already meet many next generation, star tracker/imager mission performance requirements when operated at reduced temperatures. These images also provide excellent performance at cryogenic operating temperatures appropriate to some anticipate flight missions. APS imagers with their high level of integration, on-chip timing and control, ultra-low power, and environmental robustness are excellent candidates for NASA's earth observing, interplanetary and deep space exploration missions,

Keywords: *Star* tracker, Active Pixel Sensor, APS, Radiation

1. INTRODUCTION

Star trackers (also known as star imagers) are an essential component of spacecraft attitude control systems. Modern star trackers achieve sub-pixel accuracies by centroiding defocused star images, attaining accuracies approaching a hundredth of a pixel'. [2]. The imaging devices in these star trackers are generally CCDs. However, CCDs are very sensitive to the radiation environment found in space. In particular, displacement damage, which is readily caused by proton irradiation, degrades the charge transfer efficiency (CTE) of CCDs. This, in turn, produces apparent shifts in the positions of imaged objects. The apparent shifts depend on image brightness and location within the array, making correction difficult. This has led star tracker designers to investigate alternate imagers.

The CMOS active pixel sensor (APS) has been under development for some time[3, 4]. Because it does not rely on charge transfer, it is not subject to the apparent image shifts with radiation that CCDs experience. The APS also has other benefits as a star tracker imager, including extremely low power, simple power supply demands and a high level of integration. In addition, the APS can be operated over a wide range of temperatures, down to cryogenic temperatures. It can therefore be placed in the same focal plane as an infrared array, if desired.

The present work is part of an effort to develop radiation hard active pixel sensors for star tracker applications. Unfortunately, there has been little published work on radiation effects in active pixel sensors [6, 7]. However, our own experience has been that active pixel sensors fabricated in standard, commercial CMOS processes tend *to* exhibit large increases in dark current with radiation. Likewise, the evaluation of active pixel sensors for star tracker applications has been promising, but cursory'. Active pixel sensors, in general, lag somewhat behind CCDs in performance, at least prior to irradiation.

Having been successful, as reported elsewhere, in producing active pixel sensors with a remarkable tolerance to radiation, it remained to evaluate their potential as star tracker imagers. The goal was to achieve an accuracy of ~0.01 pixels. Not having found appropriate models relating imager performance to star tracker accuracy in the literature, we have developed some. These are presented in the next section of this paper, while the remainder applies those models to measured APS results.

2. ACCURACY MODEL

2.1. General considerations

While there have been many papers published on star tracker accuracy[9-13], these have tended to take a system level perspective. The need here was for a simple model that could be used as a yardstick for evaluating detailed imager performance for star tracker applications. The model here attempts to concern itself only with imager performance, independent, for example, of optical system design. There is one exception here, however, to the extent that imager performance effects depend on the window size and the spot size. Therefore, Section 2.2 contains a brief discussion of pixelization and spot size effects.

The model is based on a simple centroid (center of mass) calculation over an $m \times m$ window. Although other algorithms have been shown to offer slightly improved position estimation performance[14], the error calculations for a centroid are straightforward and do not require the use of Monte Carlo calculations. Accuracy is calculated as RMS error, per star, per axis.

2.2. Pixelization and spot size effects

The effects of pixelization and spot size have been examined previously". The purpose of the discussion here is to establish simply the parameters to be used for the imager performance analysis. Additionally, fill factor effects are considered, since the APS, unlike the CCD, has a fill factor significantly less than one, and may have spatial non-uniformity in its response.

The error evaluated in this section is known as the algorithm bias error[11, 12]. This is the difference between the "true" star position and the estimated star position, and results from the fact that pixelization (i.e., sampling), even in the absence of noise, distorts the point spread function.

The model assumes, as in previous work, that the point spread function can be represented as a two-dimensional Gaussian:

$$I(x,y) = \frac{I_0}{2\pi\sigma_{PSF}^2} \exp\left[-\frac{(x-x_0)^2}{2\sigma_{PSF}^2}\right] \exp\left[-\frac{(y-y_0)^2}{2\sigma_{PSF}^2}\right], \tag{1}$$

where (x_0, y_0) represents the position of the "true" star image center, and σ_{PSF} is the spread of the Gaussian. For convenience, we will use as the pixel pitch as the unit of distance, with the pixels centered on the grid points. We also assume that the photosensitive area is an $h \times h$ square centered at the center of the pixel. Finally, as stated above, we compute the centroid over an $m \times m$ window, with the "true" star position somewhere in the central pixel.

In the x direction, the estimated centroid position, $\hat{x}$, is given by

$$\hat{x} = \sum_{i,j} x_{ij} U_{ij} \Big/ \sum_{i,j} U_{ij}, \tag{2}$$

where $x_{ij} = i$ is the x position of pixel (i, j), and U_{ij} is the detected signal at pixel (i, j). Calculation of $\hat{x}$ as a function of x_0 can be performed readily with a spreadsheet program, making use of the cumulative normal distribution function to calculate the pixel signals.

Because actual star positions will be random, the calculation is performed for x_0 in the range [-0.5, +0.5], and the RMS error computed. Figure 1 shows the results as a function of σ_{PSF} for various window sizes with h=l. For small values of σ_{PSF} the error is large and independent of the window size. The tightly focused spot is estimated to be in the center of whatever pixel it is in, regardless of its actual location within that pixel. As σ_{PSF} increases, the error reaches a minimum and then begins to increase slowly. This is due to uneven losses of the signal outside the window for larger spots. The minimum error decreases rapidly with increasing window size, reaching less than 0.001 pixel for a window size of only 5x5. As will be

shown in the next section, the error due to noise increases with the window size. We therefore conclude that 5×5 is the optimum window *size*, with a corresponding σ_{PSF} –0.7, and will use these parameters in further calculations.

Figure 2 shows the RMS error as a function of σ_{PSF} for various values of the photosite size, *h*, with the window size fixed at 5x5. As the photosite *size* decreases, the error increases slightly, and the minimum is shifted *to* somewhat larger values of σ_{PSF}. These changes occur rapidly and then saturate, with virtually no change beyond h=0.2. For a non-uniform sub-pixel response function we may view the output as the weighted superposition of infinitesimal photosites. Although the argument is not rigorous, it suggests that comparable bias errors can be achieved even in this case.

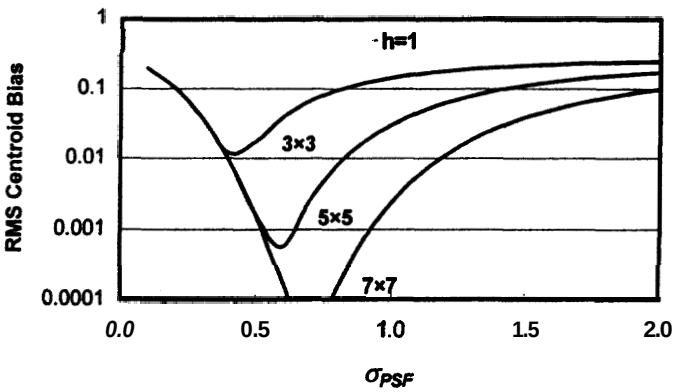

Figure 1. RMS centroid bias error as a function of spot size for various centroiding window sizes.

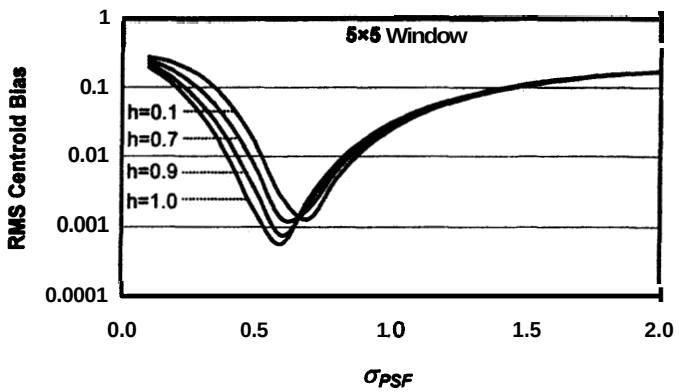

Figure 2. RMS centroid bias error as a function of spot size for different photosite sizes.

A few words are in order concerning the pixelization model and its assumptions. Although it has been argued that the 2-D Gaussian is a reasonable approximation for the *Airy* pattern, the main reason for its use here was computational simplicity. Calculations using a simple circular spot yield somewhat different results. This spot profile may more closely model a strongly defocused system, but is computationally more difficult. The bias errors are several times larger than for the 2-D Gaussian, and the characteristics of the minimum are different. The error decreases with increasing spot size until the edge of the reaches the edge of the centroiding window (r>2 for a 5×5 window), after which it increases rapidly. The optimum spot size is therefore larger than for the 2-D Gaussian. Nonetheless, an RMS error of 0.005 pixel is achieved for a 5x5 window. The performance for real image spots is probably intermediate between these.

A warning must also be made about Cassegrain type optics. The point spread function for such telescopes, when defocused, contains a hole in the center. Particularly for imagers with less than 100% fill factors, the interaction between this hole and the pixelization will produce large errors.

Finally, it must be reiterated that the error discussed in this section is a bias fiom the use of the centroid of the pixelated image as an estimate of the spot position. Use of unbiased estimators, such as Gaussian fits and maximum likelihood estimators[13-15], will avoid this error component. Even with the centroid calculation, for a known point spread function the bias can, in principle, be computed and corrected.

2.3. Noise Effects

In this section, we calculate the effects of various noise components on centroiding accuracy. We begin by assuming that the measured signal U_{ij} at pixel (i,j) consists of two components: a "true" signal, L_{ij}, and a noise or error signal, ε_{ij}, i.e. $U_{ij} = L_{ij} + \varepsilon_{ij}$. If the noise terms are small, we can determine the corruption of the centroid estimate from a differential. Defining the total signal, $L_0 = \sum_{i,j} L_{ij} \; L_0$, and the "true" centroid position, $x_0 = \sum_{i,j} x_{ij} L_{ij} \Big/ L_0$, it can be easily shown fiom a differential analysis that the centroid error due to noise is

$$\delta\hat{x} = \sum_{i,j} \left(x_{ij} - x_0\right) \varepsilon_{ij} \Big/ L_0 \tag{3}$$

We have made no assumptions so far about the ε_{ij}, except that they are small, specifically that $\sum_{i,j} \varepsilon_{ij} << \sum_{i,j} L_{ij}$. The variance of the centroid error is then

$$\sigma_{\hat{x}}^2 = \left\langle \left[\sum_{i,j} \left(x_{ij} - x_0\right) \varepsilon_{ij} \right]^2 \right\rangle \Big/ L_0^2 \;, \tag{4}$$

where $\langle \cdots \rangle$ represents the expectation value.

Equation (4) is the basis of the analysis here, and we will use it to analyze different kinds of noise, e.g. temporal *vs.* spatial, correlated *vs.* uncorrelated, constant *vs.* signal dependent. Furthermore, the calculations are analytical, without dependence on Monte Carlo simulations. These two features set the present analysis apart from previous work.

<u>Read noise</u>

Read noise is the simplest form of noise for this analysis. It is a constant, uncorrelated, temporal noise. We will assume that it has a zero mean and a single, fixed variance, σ_{RN}^2, for all pixels. The zero mean derives fiom background subtraction, which will be considered later. We need not make any further assumptions about the distribution of ε_{ij}.

Within a given image frame ε_{ij} and $\varepsilon_{i'j'}$ are uncorrelated, i.e. $\left(\varepsilon_{ij}\, \varepsilon_{i'j'}\right) = 0$, so the cross terms due to the square in (4) vanish. Equation (4) then becomes

$$\sigma_{\hat{x},RN}^2 = \frac{\sigma_{RN}^2}{L_0^2} \sum_{i,j} \left(x_{ij}^2 + \langle x_0^2 \rangle\right) \tag{5}$$

The summation in (5) depends only on the geometry of the centroiding window. Since the actual star position is unknown, x_0 should also be considered a random variable, uniformly distributed on [-0.5, 0.5]. Performing the sum for a 5×5 window, and using the fact that $\langle x_0^2 \rangle = 1/12$, we obtain the RMS error due to read noise

$$\sigma_{\hat{x},RN} = 7.2 \frac{\sigma_{RN}}{L_0} \;. \tag{6}$$

This RMS error is inversely proportional to the signal-to-noise ratio, where the signal is the total star signal over the centroiding window, and the noise is the per-pixel read noise. Any operation that increases the star signal, in particular increasing the integration time, will improve the accuracy.

Considering equation (5), as the size of the centroiding window increases, both the number of noisy samples and their moment arms increase, so that the prefactor in equation (6) scales as m^2. Thus, it is highly unfavorable, as noted in the previous section, to use an overly large centroiding window, a conclusion also reached by other authors.

Fixed pattern noise (FPN)

Fixed pattern noise (FPN) refers to a temporally constant output offset that varies in a particular spatial pattern, where the term offset implies that this noise is independent of the integration time and the signal level. The fixed pattern noise, which is fully described by specifying the offset at each pixel, can be decomposed into three components: a fully random per-pixel FPN, a per-column FPN, and a per-row FPN, the distinction being important in the summation of equation (5). We assume that all three of these FPN components are random, with variances σ^2_{PFPN}, σ^2_{CFPN}, and σ^2_{RFPN}, respectively. This excludes specific patterns, such as sinusoids, which may result from hum pickup.

Since the per-pixel FPN is fully random and uncorrelated, its mathematics are identical to those for read noise. We immediately obtain, for the 5x5 window,

$$\sigma_{\hat{x},PFPN} = 7.2\frac{\sigma_{PFPN}}{L_0} . \tag{7}$$

However for the per-column FPN all the ε_{ij} within a column are identical. After first summing over all the pixels in a column, equation (5) then becomes

$$\delta\hat{x} = m\sum_i (x_i - x_0)\varepsilon_i \Big/ L_0 . \tag{8}$$

Computing the centroiding error variance, we get

$$\sigma^2_{\hat{x},CFPN} = \frac{\sigma^2_{CFPN}}{L_0^2} m^2 \sum_i \left(x_i^2 + \left\langle x_0^2 \right\rangle\right) . \tag{9}$$

Note the sum over j has produced a factor of m^2 in (9), whereas for PFPN it produced only a factor of m. This is because the offsets in a column all add coherently, rather than randomly canceling out. For the 5x5 window we get

$$\sigma_{\hat{x},CFPN} = 16.1\frac{\sigma_{CFPN}}{L_0} . \tag{10}$$

The calculations for the per-row FPN follow identically.

Dark current non-uniformity

Imagers, in general, exhibit some dark current, and that dark current will vary from pixel to pixel. If we let σ^2_{DCNU} represent the variance of the dark rate, then the variance of the resulting error signals is $\sigma^2_{DCNU}\, t^2_{int}$, where t_{int} is the integration time. Following the same approach as for read noise, we get for the 5x5 widow

$$\sigma_{\hat{x},DCNU} = 7.2\frac{\sigma_{DCNU}\, t_{int}}{L_0} \tag{11}$$

Since L_0 is proportional to t_{int}, in this case we find that increasing the integration time does not improve the accuracy, although, of course, using a brighter star or faster optics will.

Dark current shot noise

In addition to its spatial variation, dark current is subject to shot noise, a temporal variation due to statistical fluctuations in the generation process. If we let I_{dark} represent the dark current, in electrons per second, then the dark signal will be $I_{dark}\, t_{int}$. For shot noise, the variance of the signal is equal to the mean value of the signal. Again following the same approach as for read noise, we get for the 5×5 widow

$$\sigma_{\hat{x},DCSN} = 7.2\frac{\sqrt{I_{dark}\, t_{int}}}{L_0} \tag{12}$$

In this case we find that that the centroiding error varies as $1/\sqrt{t_{int}}$.

Photoresponse non-uniformity

Inevitably, the photoresponse of an imager varies slightly from pixel to pixel. The calculation in this case is made more complex by the fact that the error signal depends on the "true" signal. Let r_{ij} represent the relative response at pixel (i, j), and let σ^2_{PRNU} be the variance of r_{ij}. Then $\varepsilon_{ij} = (r_{ij} - 1)L_{ij} = \delta r_{ij}\, L_{ij}$. Substituting in (6), and noting that the ε_{ij} are still uncorrelated from pixel to pixel, we obtain

$$\sigma^2_{\hat{x},PRNU} = \frac{\sigma^2_{PRNU}}{L_0^2}\sum_{i,j}(x_{ij} - x_0)^2 L_{ij}^2 \,. \tag{13}$$

The summation here depends only on the shape of the point spread function. For the optimum point spread function determined in the previous section we may perform the sum numerically, averaging over x_0 and y_0. We obtain

$$\sigma_{\hat{x},PRNU} = 0.20\,\sigma_{PRNU} \,. \tag{14}$$

The prefactor in (16) is independent of the centroiding window size because the summation is cut off by the fall-off of L_{ij}, and it is also surprisingly insensitive to σ_{PSF} and to the fill factor. Note that this error component is independent of the signal level.

Photon Shot Noise

Like the dark current, the star signal is also subject to shot noise. There are several stages in the collection of photoelectrons, i.e. arrival of photons at the optical aperture, transport through the optics, absorption by the detecting material and collection of the photoelectrons. Although each of these steps may be viewed as a Poisson process, with its own shot noise contribution, the overall process is also a Poisson process. We may then compute the overall shot noise from the mean detected signal, without considering the intermediate steps.

For photon shot noise, the noise values are no longer spatially uniform, making the calculation somewhat more complex. Specifically, the variance of a given ε_{ij} is just L_{ij}, using electrons as the unit of signal. Substituting this in (6), and making use of the fact that the ε_{ij} are still uncorrelated from pixel to pixel, we obtain

$$\sigma^2_{\hat{x},PSN} = \frac{1}{L_0^2}\sum_{i,j}(x_{ij} - x_0)^2 L_{ij} \,. \tag{15}$$

The numerator of (15) is just L_0 times the second moment of the point spread function. For a Gaussian profile then

$$\sigma_{\hat{x},PSN} = \frac{\sigma_{PSF}}{\sqrt{L_0}} \ . \tag{16}$$

Note that the detector performance enters this only through the effect of quantum efficiency on L_0. This error component sets a limit on possible performance,. A star position simply can not be accurately determined without an adequate supply of photons.

Background subtraction

In all of the above, it is assumed the ε_{ij} have a mean value of zero. However, real star images generally have a background due either to imager dark current or to actual astronomical background light. Failure to properly subtract the background will shift the estimated centroid position by corrupting the denominator in (2). Assuming an error ε_{bg} in the background estimate, and noting that $\sum_{i,j} x_{ij} = 0$ and $\langle x_0^2 \rangle = 1/12$, equation (6) gives us

$$\sigma^2_{\hat{x},BG} = \frac{m^2}{12} \frac{\sigma^2_{BG}}{L_0^2} \ , \tag{17}$$

or equivalently, for the 5×5 window

$$\sigma_{\hat{x},BG} = 1.44 \frac{\sigma_{BG}}{b} \ . \tag{18}$$

Typically, the background level is estimated fiom the $(m+2)^2 - m^2$ pixels forming a ring around the centroiding window. Assuming these have an RMS noise σ_0, which we may assume to be equal to the largest noise term, we obtain for the 5×5 window

$$\sigma_{\hat{x},BG} = 0.29 \frac{\sigma_0}{L_0} \ . \tag{19}$$

Because the prefactor is so small, background subtraction error will almost never be a significant contributor to the total error budget.

Table I
Summary of accuracy model

Noise Component	Formula	5×5	t_{int} dependence
Read Noise	$\sigma^2_{\hat{x},RN} = \frac{\sigma^2_{RN}}{L_0^2}\sum_{i,j}\left(x_{ij}^2 + \langle x_0^2\rangle\right)$	$\sigma_{\hat{x},RN} = 7.2\frac{\sigma_{RN}}{L_0}$	$1/t_{int}$
Per-Pixel FPN	$\sigma^2_{\hat{x},PFPN} = \frac{\sigma^2_{PFPN}}{L_0^2}\sum_{i,j}\left(x_{ij}^2 + \langle x_0^2\rangle\right)$	$\sigma_{\hat{x},PFPN} = 7.2\frac{\sigma_{PFPN}}{L_0}$	$1/t_{int}$
Per-Column FPN	$\sigma^2_{\hat{x},CFPN} = \frac{\sigma^2_{CFPN}}{L_0^2}m^2\sum_{i}\left(x_i^2 + \langle x_0^2\rangle\right)$	$\sigma_{\hat{x},CFPN} = 16.1\frac{\sigma_{CFPN}}{L_0}$	$1/t_{int}$
Dark Current Non-Uniformity	$\sigma^2_{\hat{x},DCNU} = \frac{\sigma^2_{DCNU}t^2_{int}}{L_0^2}\sum_{i,j}\left(x_{ij}^2 + \langle x_0^2\rangle\right)$	$\sigma_{\hat{x},DCNU} = 7.2\frac{\sigma_{DCNU}t_{int}}{L_0}$	independent
Dark Current Shot Noise	$\sigma^2_{\hat{x},DCSN} = \frac{I_{dark}t_{int}}{L_0^2}\sum_{i,j}\left(x_{ij}^2 + \langle x_0^2\rangle\right)$	$\sigma_{\hat{x},DCSN} = 7.2\frac{\sqrt{I_{dark}t_{int}}}{L_0}$	$1/\sqrt{t_{int}}$
Photoresponse Non-Uniformity	$\sigma^2_{\hat{x},PRNU} = \frac{\sigma^2_{PRNU}}{L_0^2}\sum_{i,j}\left(x_{ij} - x_0\right)^2 L_{ij}^2$	$\sigma_{\hat{x},PRNU} = 0.20\,\sigma_{PRNU}$	independent
Photon Shot Noise	$\sigma^2_{\hat{x},PSN} = \frac{1}{L_0^2}\sum_{i,j}\left(x_{ij} - x_0\right)^2 L_{ij}$	$\sigma_{\hat{x},PSN} = \frac{\sigma_{PSF}}{\sqrt{L_0}}$	$1/\sqrt{t_{int}}$
Background Subtraction	$\sigma^2_{\hat{x},BG} = \frac{m^2}{12}\frac{\sigma^2_{BG}}{L_0^2}$	$\sigma_{\hat{x},BG} = 1.44\frac{\sigma_{BG}}{L_0}$	$1/t_{int}$

3. ACTIVE PIXEL SENSORS

3.1. APS description

CMOS Active Pixel Sensors come in many varieties, but have the common feature that each pixel contains a photosite, an amplifier and a select switch for analog multiplexing. This sets the APS apart from the CCD, where the signal is read out by repeated shifting. Because there is no charge shifting, the APS is not susceptible to the CTE degradation that besets CCDs in a space radiation environment. On the other hand, the multiplexing scheme often produces increased fixed pattern noise, particularly per-column fixed pattern noise.

The photosite in an APS may be either a photogate or a photodiode, each having its own advantages. Likewise, a large variety of amplifier and multiplexer designs are, in principle, possible. However, since the pixel amplifier and select switch take up space in the pixel at the expense of the photosite, reducing the fill factor, a simple source follower amplifier and pass transistor are generally used.

Because the APS is made in a standard CMOS process, a full range of analog and digital processing circuits are available, including analog-to-digital converters. It also allows the leveraging of the large volume of CMOS business for the process development and maintenance costs. In particular, considerable resources have been devoted to the development of radiation hard CMOS processes, and these are available for APS fabrication.

In response to the need for imagers for high radiation space environments, particularly for star tracking applications, JPL has investigated radiation effects in active pixel sensors, and the opportunities for radiation hardening. An active pixel sensor, designated RHAPS, was designed and fabricated in the Lockheed-Martin RHCMOS-5M process. This is a radiation hard,

0.5 pm, single poly, triple metal process. This imager and its performance will be analyzed for star tracker applications based on the models developed in the first part of this paper.

The RHAPS is described more fully elsewhere[16], but a brief summary is given here. The imager format is a 256x256 photodiode array, with a 20 μm pitch. The relatively large pitch was chosen to allow for a good fill factor while including a variety of layout features hoped to improve radiation performance. A fill factor of 47% was achieved. The photodiode was chosen because experience had shown that photodiodes are less sensitive to radiation than are photogates. Double-Delta sampling was used to reduce the per-column fixed pattern noise. The RHAPS is "smart" chip, with full timing and control integrated on chip. The imaging window and integration time are programmable through a set of registers. However, the RHAPS does not include an analog-to-digital converter; only analog output is available.

3.2. RHAPS performance

The performance of the RHAPS is summarized in Table II for 5 V operation at room temperature. The RHAPS was designed to operate at either 5 V or 3.3 V. Operation at 3.3 V results in lower dark current, but also a lower full well capacity. Total power consumption is less than 20 mW.

The dark current is surprisingly high in these devices, corresponding to 60 nA/cm^2. This is two orders of magnitude larger than dark currents seen on imagers fabricated in standard commercial processes, and is believed to have resulted from problems during wafer processing. Test structure results show that this dark current is proportional to the diode perimeter. A second run is being submitted to test this hypothesis.

Figure 3 shows the error components computed fiom the accuracy model using the pre-radiation, room temperature results in Table 11, where the horizontal axis is the total collected signal per star, L_0, measured in electrons. The corresponding visual star magnitude is shown for reference on the upper axis, based on a nominal optical system design, i.e. a 5 cm aperture, 100 ms integration time, 50% optical throughput and 30% effective quantum efficiency.

It is clear that, by far, the largest contributor to the error is the dark current non-uniformity. Fortunately, the dark current can be reduced by cooling, and measurements support the usual activation energy of ~0.55 eV. This implies that the DCNU component can be reduced below the PFPN component already at –35° C, a temperature attainable with thermoelectric cooling.

With dark current non-uniformity and dark current shot noise eliminated by cooling, the next most significant error component is due to the per-column fixed pattern noise, limiting the performance to ~0.01 pixel at M_v=2.5 or ~0.1 pixel at M_v=4.5. Investigations are under way to determine if the CFPN, which is ~0.1% of full scale can be further improved, but this performance is already comparable to other APS devices. Although fixed pattern noises, and even dark current non-uniformity, are in principle correctable by subtracting dark frames, this is not considered practical in most star trackers, since a shutter would be required. However, it should be possible to measure and correct per-column fixed pattern noise by use of a dummy row, in which the signal is forced to be zero.

Although the read noise is not a major factor in the error budget at this time, it is still relatively large compared to other imagers, particularly CCDs. The read noise is mostly attributable to reset noise, also known as kTC noise, and it is large because the RHAPS contains a rather large photodiode. In addition to the use of smaller photodiodes in future generations, we are investigating the possibility of off-chip correlated double sampling (CDS) to reduce this noise.

It is seen that the photoresponse non-uniformity is a negligible contributor to centroiding error. The remarkably good PRNU reported here is a local PRNU, taken from the variances of 8×8 windows in a flat field. This is the appropriate measure for centroiding operations.

Finally, there is one error component which was not analyzed in the model above, that due to nonlinearity, because nonlinearity is very difficult to parameterize. The nonlinearity of the RHAPS is relatively large, with the conversion gain decreasing from 2 μV/e$^-$ for small signals to – 1μV/e$^-$ near saturation. This is because of the doping profiles in this particular process, and because the signal swings are large compared to the bias voltages. We performed simulations of centroiding error similar to those described above, using the measured RHAPS nonlinearity. It is found that the RMS error is –0.003 pixel when the central pixel reaches saturation, and only 0.01 pixel at ten times this level. This relies on the fact that the APS is extremely resistant to blooming. Thus, nonlinearity is not an issue for centroiding accuracy. Nonlinearity can, in any case, be calibrated out

Table II
RHAPS Performance

Parameter	Value	Conditions
Peak Quantum Efficiency	~50%	500 nm
Conversion Gain	2.0 μV/e⁻	small signal
Full Well	800,000 e⁻	5 V
Read Noise	200 e⁻	
Dark Current	$1.5 \cdot 10^{7}$ e⁻/s $3.8 \cdot 10^{6}$ e⁻/s	Pre-rad, room temperature, 5 V 5 Mrad, room temperature, 5 V
Dark Current Non-Uniformity	$1.5 \cdot 10^{3}$ e⁻/s	Re-rad, room temperature, 5 V
Per-Pixel Fixed Pattern Noise	100 e⁻	
Per-Column Fixed Pattern Noise	500 e⁻	
Photoresponse Non-Uniformity	0.8%	

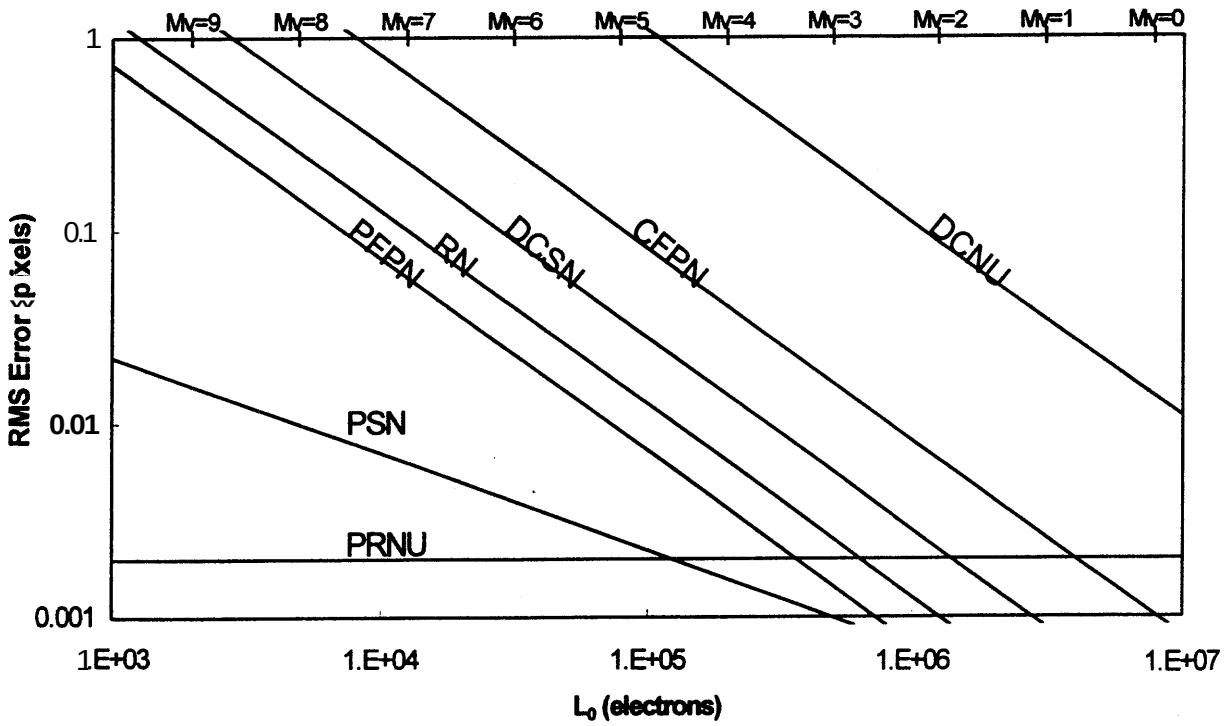

Figure 3. RMS centroid error components as a function of star signal for the RHAPS. Star magnitudes are based on a nominal optical system design

3.3. Radiation Testing

Details of the radiation testing of the **RHAPS** are described elsewhere, but are summarized here. Testing was performed unbiased with Co^{60} to 5 Mrad, biased/operating with Co^{60} to 2 Mrad, and unbiased with 63 MeV protons to $1.2 \cdot 10^{12}$ p^{+}/cm^{2}. For the Co^{60} exposures. the only significant change was an increase in the dark current, with little difference between the biased and unbiased cases. The dark current increase was approximately linear with dose, and corresponds to approximately 18 $pA/cm^{2}/krad$ for 5 V operation. This low value is comparable to the dark current increase to be expected from displacement damage in a space proton radiation environment. The displacement damage dark current is not very amenable to radiation hardening efforts, and so represents a floor for radiation performance.

It was also found that the dark current nonuniformity did not increase measurably with Co^{60} irradiation. This is probably because the dark current nonuniformity is dominated by the nonuniformity of the initial, high dark current. This is significant

because it implies, fiom Fig. 3, that the accuracy will not be degraded by radiation. This should also apply in the case that process improvements decrease the initial dark current, although we have on other APS imagers, observed some increase in dark current nonuniformity with radiation.

Finally, no measurable change was observed with proton irradiation. In particular, no increase was seen in the number of hot pixels. Again, these effects are probably present to some smaller degree, but are masked by the high initial dark current.

4. CONCLUSIONS

The RHAPS has demonstrated an ,ability to operate from a single power supply at very low power and over a wide temperature range, from room temperature to cryogenic conditions, and to very high radiation levels. These are all highly valuable assets for space applications. The RHAPS has been evaluated using the star tracker accuracy model developed here, and it is found that, with moderate cooling, it can achieve 0.1 pixel accuracy for stars of visual magnitude – 5, depending on system details. This performance is already useful for many space applications, and anticipated process and design improvements should improve this performance further, providing improved accuracy for fainter stars and relaxing cooling requirements.

ACKNOWLEDGMENTS

The research described in this paper was carried out at the Jet Propulsion Laboratory, California Institute of Technology, and was sponsored by Air Force Space Missile Command and National Aeronautics and Space Administration. The authors would also like to thank Capt. Kevin Carrow, Maj. Tom Grycewicz, and Maj. Chris McCormack, and Dr. John Boyle for their support of the radiation hardened CMOS imager development efforts.

REFERENCES

1. A.R. Eisenman and C.C. Liebe, "The Advancing State-of-the Art in Second Generation Star Trackers", *IEEE Aerospace Conf.*, 1, pp. 111-118, 1998.
2. C.C. Liebe, "Star Trackers for Attitude Determination", *IEEE AES Systems Mag.*, 10, pp. 10-16, 1995.
3. E.R. Fossum, "CMOS image sensors: Electronic camera-on-a-chip," *IEEE Trans. on Electron Devices*, vol. 44, pp. 1689-1698, 1997.
4. S.K. Mendis, S.E. Kemeny, B. Pain, R.C. Gee, Q. Kim, and E.R. Fossum, "CMOS active pixel image sensors for highly integrated imaging systems," *IEEE J. of Solid-state Circuits*, vol. 32, pp. 187-198, 1997.
5. B.R. Hancock and G.A. Soli, "Total dose testing of a CMOS charged particle spectrometer", *IEEE Trans. Nuc. Sci.*, 44, pp. 1957-1964, 1997.
6. M. Cohen and J.P. David, "Radiation Induced Dark Current in CMOS Active Pixel Sensors", *IEEE Trans. Nuc. Sci.*, 47, pp. 2485-2491, 2000.
7. G. R. Hopkinson, "Radiation effects in a CMOS active pixel sensor," *IEEE Trans. Nuc. Sci.*, 47, pp. 2480-2484, 2000.
8. C.C. Liebe, E.W. Dennison, B. Hancock, R.C. Stirbl and B. Pain, "Active Pixel Sensor (APS) Based Star Tracker", *IEEE Aerospace Conf.*, 1, pp. 119-127, 1998.
9. P.M. Salomon and T.A. Glavich, "Image Signal Processing in Sub-Pixel Accuracy Star Trackers", in Smart Sensors II, *Proc. SPIE*, 252, pp. 64-74, 1980.
10. J.P. Fillard, "Subpixel Accuracy Location Estimation from Digital Signals", *Optical Eng.*, 31, pp. 2465-2471, 1992.
11. S.B. Grossman and R.B. Emmons, "Performance Analysis and Size Optimization of Focal Planes for Point-Source Tracking Algorithm Applications", *Optical Eng.*, 23, pp. 167-176, 1984.
12. B.F. Alexander and K.C. Ng, "Elimination of Systematic Error in Subpixel Accuracy Centroid Estimation", *Optical Eng.*, 30, pp. 1320-1330, 1991.
13. K.A. Winick, "Cramer-Rao Lower Bounds on the Performance of Charge-Coupled-Device Optical Position Estimators", *J. Optical Soc. Am. A*, 3, pp. 1809-1815, 1986.
14. R.C. Stone, "A Comparison of Digital Centering Algorithms", *Astron. J.*, 97, pp. 1227-1237, 1989.
15. C-L Lu, "Digital Image Centering with the Maximum Likelihood Method", *Astron. Astrophys*, 275, pp. 349-352, 1993.
16. B.R. Hancock, T.J. Cunningham, K. McCarty, G. Yang, C. Wrigley, P.G. Ringold. R.C. Stirbl, and B. Pain, "Multi-Megarads(Si) Radiation Tolerant Integrated CMOS Imager", *SPIE Photonics West*, 2001.